PHYSICAL REVIEW D **87,** 054014 (2013)

Explanation of systematics of CMS p + Pb high multiplicity dihadron data at $\sqrt{s_{\rm NN}} = 5.02$ TeV

Kevin Dusling[1] and Raju Venugopalan[2]

[1]*Physics Department, North Carolina State University, Raleigh, North Carolina 27695, USA*
[2]*Physics Department, Brookhaven National Laboratory, Upton, New York 11973, USA*

(Received 20 November 2012; published 12 March 2013)

In a recent article [K. Dusling and R. Venugopalan, arXiv:1210.3890 [Phys. Rev. D (to be published)]], we showed that high multiplicity dihadron proton-proton (p + p) data from the CMS experiment are in excellent agreement with computations in the color glass condensate effective field theory. This agreement of the theory with several hundred data points provides a nontrivial description of both nearside (''ridge'') and awayside azimuthal collimations of long range rapidity correlations in p + p collisions. Our prediction in Dusling and Venugopalan [arXiv:1210.3890 [Phys. Rev. D (to be published)]] for proton-lead (p + Pb) collisions is consistent with results from the recent CMS p + Pb run at $\sqrt{s_{\rm NN}} = 5.02$ TeV for the largest track multiplicity $N_{\rm track} \sim 40$ we considered. The CMS p + Pb data shows the following striking features: (i) a strong dependence of the ridge yield on $N_{\rm track}$, with a significantly larger signal than in p + p for the same $N_{\rm track}$, (ii) a stronger p_T dependence than in p + p for large $N_{\rm track}$, and (iii) a nearside collimation for large $N_{\rm track}$ comparable to the awayside for the lower $p_T = p_T^{\rm trig} = p_T^{\rm assoc}$ dihadron windows. We show here that these systematic features of the CMS p + Pb di-hadron data are all described by the color glass condensate (with parameters fixed by the p + p data) when we extend our prediction in Dusling and Venugopalan [arXiv:1210.3890 [Phys. Rev. D (to be published)]] to rarer high multiplicity events. We also predict the azimuthally collimated yield for yet unpublished windows in the $p_T^{\rm trig}$ and $p_T^{\rm assoc}$ matrix.

DOI: 10.1103/PhysRevD.87.054014 PACS numbers: 13.85.Ni

I. INTRODUCTION

Rapidity separated dihadron correlations in high multiplicity events at the LHC offer subfemtoscopic scale snapshots of rare configurations constituting the structure of matter in the colliding hadrons. A largely unexpected discovery at the LHC by the CMS collaboration in high multiplicity $N_{\rm track} > 110$ proton-proton (p + p) events [1] was a collimation in the azimuthal ''nearside'' separation ($\Delta\phi \approx 0$) between charged hadrons that have rapidity separations $2 \leq |\Delta\eta| \leq 4$. For recent reviews on this nearside ''ridge'' effect, see Refs. [2,3]. In Ref. [4], we showed that this ridge could be explained by ''glasma graphs'' [5–7] that arise in the color glass condensate (CGC) effective field theory (EFT) [8]. When the phase space density of gluons in the proton's wave function reach maximal occupancy, or saturation, these graphs are significantly enhanced in high multiplicity events relative to minimum bias by α_S^{-8}, a factor of 10^4–10^5 for typical values of α_S. This enhancement is a remarkable illustration of how the power counting changes in different dynamical regions of the EFT.

Recently, we extended this study significantly [9], and showed that a combination of saturation [10,11] and Balitsky-Fadin-Kuraev-Lipatov (BFKL) dynamics [12,13] in the CGC EFT provides an excellent description of several hundred data points comprising a matrix (in uniformly spaced windows in the dihadron momenta $p_T^{\rm trig}$ and $p_T^{\rm asc}$) of the associated dihadron yield per trigger versus $\Delta\phi$. A novel feature of this study was the demonstration that BFKL dynamics, which generates gluon emissions between the gluons that fragment into triggered hadrons, does an excellent job describing the awayside spectra. The description is significantly better than PYTHIA-8 [1], and $2 \to 4$ QCD graphs in the quasi-multi–Regge-kinematics, both of which overestimate the awayside yield, especially at larger momenta.

In Ref. [9], we also made a prediction for the ridge and the awayside collimation in proton-lead collisions at $\sqrt{s_{NN}} = 5.02$ TeV at the LHC. However, as we shall discuss in detail, the prediction corresponded to a value of $N_{\rm track} \sim 40$ for p + Pb collisions. The magnitude of the signal is comparable to that in p + p collisions at $N_{\rm track} \sim 100$. Dihadron data from the p + Pb run at the LHC at $\sqrt{s_{NN}} = 5.02$ TeV are now available [14] and results are available for multiplicities much larger than those considered in Ref. [9]. These data show the following remarkable features. (i) They exhibit a strong dependence on the number of charged hadron tracks [15], labeled $N_{\rm trk}^{\rm offline}$ by the CMS collaboration. In particular, it is observed that the associated dihadron yield per trigger in p + Pb is significantly larger than the same signal at the same value of $N_{\rm trk}^{\rm offline}$ in p + p collisions. (ii) Second, they observe a distinct p_T ($p_T^{\rm trig} \sim p_T^{\rm asc}$) dependence of the collimated yield which is peaked around the same values of p_T in both p + p and p + Pb collisions, but drops off much faster in p + Pb with increasing p_T. (iii) Finally, the dihadron yield, as a function of $\Delta\phi$, is nearly as high on the nearside as on the awayside for low values of p_T, indicating that the

long range in $\Delta\eta$ awayside dijet signal is suppressed relative to the glasma graph contribution.

In this paper, we will show that all these novel features of the p + Pb data can be explained systematically in the color glass condensate framework. The parameters in the computations are fixed to be identical to those in our study of p + p collisions in Ref. [9], with the exception being the values of the scale $Q_0(y_0)$ (whose meaning we shall discuss further) in the proton and lead nuclei. These are varied at an initial rapidity y_0 to take into account the different geometry of lead nuclei relative to that of the projectile proton. If the systematics of the signal were not reproduced by varying the Q_0's of proton and lead nuclei, there is little freedom left in the framework to vary something else to obtain it.

The paper is organized as follows. In the next section, we will present the formulae used in the computation of glasma and BFKL graphs. Since all details have been discussed previously in Ref. [9] and references therein, we will reintroduce them briefly only for completeness, our focus here being the understanding of the systematics of the new CMS p + Pb data. In Sec. III, we will discuss in detail results in the CGC, compare these to the data, and make predictions for as yet unpublished data. In the final section, we will summarize our conclusions, discuss alternative interpretations and further refinements and tests of the CGC framework.

II. GLASMA AND BFKL CONTRIBUTIONS IN THE CGC EFT

The collimated correlated two-gluon production glasma and BFKL graphs are illustrated in Fig. 1. The collimated contributions from all the glasma graphs can be compactly written as

$$\frac{d^2N^{\rm corr}_{\rm Glasma}}{d^2\mathbf{p}_T d^2\mathbf{q}_T dy_p dy_q} = \frac{\alpha_S(\mathbf{p}_T)\alpha_S(\mathbf{q}_T)}{4\pi^{10}} \frac{N_C^2}{(N_C^2-1)^3\zeta} \frac{S_\perp}{\mathbf{p}_T^2\mathbf{q}_T^2} K_{\rm glasma}\left[\int_{\mathbf{k}_T}(D_1+D_2) + \sum_{j=\pm}\left(A_1(\mathbf{p}_T, j\mathbf{q}_T) + \frac{1}{2}A_2(\mathbf{p}_T, j\mathbf{q}_T)\right)\right], \quad (1)$$

where we have defined

$$\begin{aligned} D_1 &= \Phi^2_{A_1}(y_p,\mathbf{k}_T)\Phi_{A_2}(y_p,\mathbf{p}_T-\mathbf{k}_T)[\Phi_{A_2}(y_q,\mathbf{q}_T+\mathbf{k}_T)+\Phi_{A_2}(y_q,\mathbf{q}_T-\mathbf{k}_T)],\\ D_2 &= \Phi^2_{A_2}(y_q,\mathbf{k}_T)\Phi_{A_1}(y_p,\mathbf{p}_T-\mathbf{k}_T)[\Phi_{A_1}(y_q,\mathbf{q}_T+\mathbf{k}_T)+\Phi_{A_1}(y_q,\mathbf{q}_T-\mathbf{k}_T)]. \end{aligned} \quad (2)$$

These four terms, called the "single diffractive" and "interference" graphs in Ref. [5], constitute the leading $\mathbf{p}_T/Q_S$ behavior. Also included is the next order correction in $\mathbf{p}_T/Qs$ where we have [16] $A_1 = \delta^2(\mathbf{p}_T+\mathbf{q}_T)[\mathcal{I}_1^2+\mathcal{I}_2^2+2\mathcal{I}_3^2]$, such that

$$\begin{aligned} \mathcal{I}_1 &= \int_{\mathbf{k}_{1\perp}} \Phi_{A_1}(y_p,\mathbf{k}_{1\perp})\Phi_{A_2}(y_q,\mathbf{p}_T-\mathbf{k}_{1\perp})\frac{(\mathbf{k}_{1\perp}\cdot\mathbf{p}_T-\mathbf{k}_{1\perp}^2)^2}{\mathbf{k}_{1\perp}^2(\mathbf{p}_T-\mathbf{k}_{1\perp})^2},\\ \mathcal{I}_2 &= \int_{\mathbf{k}_{1\perp}} \Phi_{A_1}(y_p,\mathbf{k}_{1\perp})\Phi_{A_2}(y_q,\mathbf{p}_T-\mathbf{k}_{1\perp})\frac{|\mathbf{k}_{1\perp}\times\mathbf{p}_T|^2}{\mathbf{k}_{1\perp}^2(\mathbf{p}_T-\mathbf{k}_{1\perp})^2},\\ \mathcal{I}_3 &= \int_{\mathbf{k}_{1\perp}} \Phi_{A_1}(y_p,\mathbf{k}_{1\perp})\Phi_{A_2}(y_q,\mathbf{p}_T-\mathbf{k}_{1\perp})\frac{(\mathbf{k}_{1\perp}\cdot\mathbf{p}_T-\mathbf{k}_{1\perp}^2)|\mathbf{k}_{1\perp}\times\mathbf{p}_T|}{\mathbf{k}_{1\perp}^2(\mathbf{p}_T-\mathbf{k}_{1\perp})^2}. \end{aligned}$$

The other contribution, A_2, in Eq. (1) can be expressed as

$$\begin{aligned} A_2 = \int_{\mathbf{k}_{1\perp}} &\Phi_{A_1}(y_p,\mathbf{k}_{1\perp})\Phi_{A_1}(y_p,\mathbf{k}_{2\perp})\Phi_{A_2}(y_q,\mathbf{p}_T-\mathbf{k}_{1\perp})\Phi_{A_2}(y_q,\mathbf{q}_T+\mathbf{k}_{1\perp})\\ &\times\frac{(\mathbf{k}_{1\perp}\cdot\mathbf{p}_T-\mathbf{k}_{1\perp}^2)(\mathbf{k}_{2\perp}\cdot\mathbf{p}_T-\mathbf{k}_{2\perp}^2)+(\mathbf{k}_{1\perp}\times\mathbf{p}_T)(\mathbf{k}_{2\perp}\times\mathbf{p}_T)}{\mathbf{k}_{1\perp}^2(\mathbf{p}_T-\mathbf{k}_{1\perp})^2}\\ &\times\frac{(\mathbf{k}_{1\perp}\cdot\mathbf{q}_T-\mathbf{k}_{1\perp}^2)(\mathbf{k}_{2\perp}\cdot\mathbf{q}_T-\mathbf{k}_{2\perp}^2)+(\mathbf{k}_{1\perp}\times\mathbf{q}_T)(\mathbf{k}_{2\perp}\times\mathbf{q}_T)}{\mathbf{k}_{2\perp}^2(\mathbf{q}_T+\mathbf{k}_{1\perp})^2}, \end{aligned} \quad (3)$$

where $\mathbf{k}_{2\perp}\equiv\mathbf{p}_T-\mathbf{q}_T-\mathbf{k}_{1\perp}$. The above expressions are the result of including all combinatorial combinations of graphs represented by the Feynman diagram to the left in Fig. 1. The combinatorics is a result of different ways of averaging over strong color sources between the amplitude and complex conjugate amplitude in both projectile and target.

In Eqs. (1)–(3) the only function (besides the one loop running coupling constant α_S) is the unintegrated gluon distribution (UGD) per unit transverse area

$$\Phi_A(y,k_\perp) = \frac{\pi N_C k_\perp^2}{2\alpha_S}\int_0^\infty dr_\perp r_\perp J_0(k_\perp r_\perp)[1-\mathcal{T}_A(y,r_\perp)]^2, \quad (4)$$

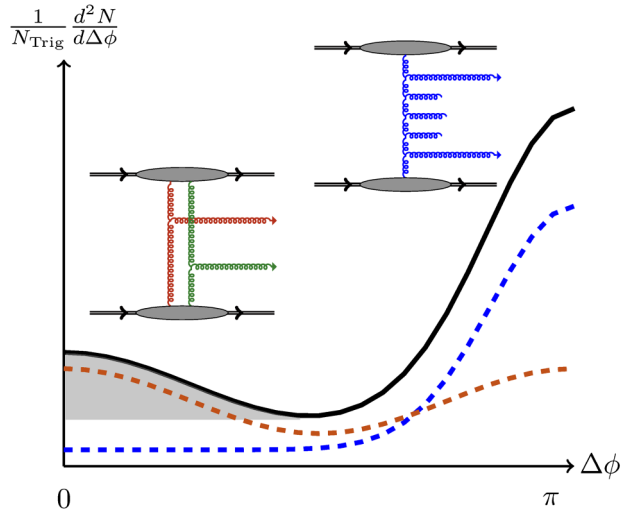

FIG. 1 (color online). Anatomy of dihadron correlations. The glasma graph is on the left and its schematic contribution to the double inclusive cross section is shown as the dashed orange curve. On the right is the back-to-back graph and the shape of its yield (dashed blue curve). The grey blobs denote emissions all the way from beam rapidities to those of the triggered gluons. The solid black curve represents the sum of contributions from glasma and back-to-back graphs. The shaded region represents the associated yield calculated using the zero-yield-at-minimum (ZYAM) procedure. Figure from Ref. [9].

where $\mathcal{T}_A$ is the forward scattering amplitude of a quark-antiquark dipole of transverse size $r_\perp$ on the target A; it, or equivalently, the UGD, is a universal quantity that can be determined by solving the Balitsky-Kovchegov (BK) equation [17,18] as a function of the rapidity $y = \log(x_0/x)$. The forward scattering amplitude $\mathcal{T}_A(y, r_\perp)$ at the initial scale $x = x_0$ is a dimensionless function of $r_\perp^2 Q_0^2$, where Q_0 is a nonperturbative scale at the initial rapidity. The saturation scale Q_S, defined as the transverse momentum defining the peak value of Φ on the left-hand side of Eq. (4), is typically a larger scale even at the initial rapidity, and grows rapidly via the BK renormalization group equation with rapidity. In the BK equation, different impact parameters in the proton/nuclear target are modeled by varying Q_0. The minimum-bias (median impact parameter) value we choose for the proton $Q_0^2 = 0.168$ GeV^2 (corresponding to a $Q_S \approx 0.7$ GeV in the adjoint representation *at the initial rapidity*), is the value that gives a best fit to deeply inelastic electron-proton scattering data from HERA [19].

In Eq. (1), the two parameters which are held fixed in p + p and p + Pb are the transverse overlap area $S_\perp$ and the nonperturbative constant $\zeta = 1/6$, which as discussed further below, specifies the correction to the k_T factorized UGD description due to soft multigluon interactions. It is independently constrained by p + p multiplicity distributions [20,21] and real time classical Yang-Mills computations [22].

The framework of glasma graphs is based on the factorization theorems derived in Ref. [23], which include leading log corrections to all orders in perturbation theory (so-called LLx approximation) as well as all leading multiple scattering contributions. As the full expression is very cumbersome, a Gaussian truncation is employed in Ref. [6], where Eq. (1) was first derived. The Gaussian truncation was shown in Ref. [24] to be a very good approximation to the full JIMWLK evolution. In addition, it is assumed that $Q_S < \mathbf{k}_T$, in order to obtain the expression in terms of UGDs (unintegrated gluon distributions). We emphasize that the resulting expression cannot be interpreted simply as the product of UGDs with matrix elements, but combines LLx contributions to each. What we use for the UGDs is the running coupling Balitsky-Kovchegov equation, which includes all LLx contributions to the UGDs + running coupling NLLx effects via the Balitsky prescription [25].

A state of the art computation of the glasma graphs would include NLLx evolution along with all multiple scattering contributions. This is unfortunately not available at present. As noted, what we have in Eq. (1) is LLx with some fraction of the NLLx contribution that corresponds to running coupling. In addition, we are using UGDs instead of the full multiple scattering contribution which would need large scale numerical simulations. The parameter ζ is a nonperturbative constant that accounts for corrections due to multiple scattering when $Q_S \gtrsim k_T$. These were computed previously for purely classical double inclusive gluon production [22,26] and the value of ζ extracted in those computations is compatible with the value of one sixth we have used in our p + p and p + A results. This value of ζ is also independently constrained by p + p multiplicity distributions [20,21]. We note further that the collimated structures seen in the perturbative *classical* computations persist in the full nonperturbative classical results, thereby lending confidence that these latter primarily renormalize the amplitude of the former.

We now turn to the double inclusive distribution from the back-to-back BFKL graphs shown in Fig. 1. The double inclusive multiplicity can be expressed as [27,28]

$$\frac{d^2N^{\rm corr}_{\rm BFKL}}{d^2\mathbf{p}_T d^2\mathbf{q}_T dy_p dy_q} = \frac{32N_c\alpha_s(\mathbf{p}_T)\alpha_s(\mathbf{q}_T)}{(2\pi)^8 C_F}\frac{S_\perp}{\mathbf{p}_T^2\mathbf{q}_T^2}K_{\rm bfkl} \times \int_{\mathbf{k}_{0\perp}}\int_{\mathbf{k}_{3\perp}} \Phi_A(x_1,\mathbf{k}_{0\perp})\Phi_B(x_2,\mathbf{k}_{3\perp})\mathcal{G}(\mathbf{k}_{0\perp}-\mathbf{p}_T,\mathbf{k}_{3\perp}+\mathbf{q}_T,y_p-y_q), \quad (5)$$

where $\mathcal{G}$ is the BFKL Green's function

$$\mathcal{G}(\mathbf{q}_{a\perp}, \mathbf{q}_{b\perp}, \Delta y) = \frac{1}{(2\pi)^2} \frac{1}{(\mathbf{q}_{a\perp}^2 \mathbf{q}_{b\perp}^2)^{1/2}} \sum_n e^{in\bar{\phi}} \times \int_{-\infty}^{+\infty} d\nu e^{\omega(\nu,n)\Delta y} e^{i\nu \ln(\mathbf{q}_{a\perp}^2/\mathbf{q}_{b\perp}^2)}. \quad (6)$$

Here $C_F = (N_C^2 - 1)/2N_c$, $\omega(\nu, n) = -2\bar{\alpha}_s \mathrm{Re}[\Psi(\frac{|n|+1}{2} + i\nu) - \Psi(1)]$ is the BFKL eigenvalue, where $\Psi(z) = d\ln\Gamma(z)/dz$ is the logarithmic derivative of the Gamma function. Further, we have $\bar{\alpha}_s \equiv N_c \alpha_S(\sqrt{\mathbf{q}_{a\perp}\mathbf{q}_{b\perp}})/\pi$ and $\bar{\phi} \equiv \arccos(\frac{\mathbf{q}_{a\perp}\cdot\mathbf{q}_{b\perp}}{|\mathbf{q}_{a\perp}||\mathbf{q}_{b\perp}|})$.

The description of the awayside jet in the above BFKL framework is also LLx with running coupling corrections, whereby, as for the glasma graphs, the UGD evolution is described by the running coupling Balitsky-Kovchegov equation. NLLx corrections to this framework has been computed in Ref. [27]. There it was demonstrated that the NLLx correction to the $\Delta\Phi$ independent pedestal is large (a factor 2 to 3). However, the NLLx contribution to the collimated $\langle\cos(\Delta\Phi)\rangle$ and $\langle\cos(2\Delta\Phi)\rangle$ moments, which are the quantities of interest here, is 10%–30%, of which, we expect, the running coupling will account for a good fraction. Hence, based on the results in these works, it is reasonable to conclude that the BFKL contribution to the collimated yield has 10%–30% uncertainties, in line with the K_{bfkl} values employed in this work.

As shown in Fig. 1, Eq. (5) gives a collimated $\Delta\Phi$ contribution exclusively on the awayside, peaked at $\Delta\Phi = \pi$, while Eq. (1) gives a "dipole" $\cos(2\Delta\Phi)$-like contributions with maxima at 0 and π. It is the interplay between these contributions with varying Q_0 in projectile and target that describes the systematics of the proton-proton and proton-lead data, that we shall now discuss further.

The two K factors used throughout this work are introduced to take into account not only uncertainties in higher order computations but also acceptance corrections and uncertainties in the choice of fragmentation functions and hadronization. There is no reason *a priori* why all these should be the same in p + p and p + A. Also, modulo a better understanding of the multiplicity distribution in p + A, some of the uncertainties in K factors could be absorbed in the initial saturation scale Q_0, corresponding to slightly different number of participants. A systematic study of these, along with data from ALICE and ATLAS will be reported in a forthcoming work. In addition to data on multiplicity distributions in the rapidity window of interest, uncertainties on fragmentation functions in particular can be constrained by forthcoming data from the LHC on single particle spectra at forward rapidities. Given these uncertainties, the fact that both K factors are of order unity and able to explain dihadron data from p + p to p + Pb (results for which we will now discuss) for different centralities and p_T selections is remarkable.

III. RESULTS

As noted, all parameters in Eqs. (1) and (5) are identical to those describing the proton-proton data. To simulate the p + Pb collision, all we do is vary Q_0^2 in the proton and lead nuclei. The proton Q_0^2 is varied in multiples of the "minimum bias" value of $Q_0^2 = 0.168\ \mathrm{GeV}^2$ to simulate events that probe more central impact parameters in the proton, where the gluon density is considerably higher than the gluon density for the median impact parameter corresponding to minimum-bias events. Likewise, we define the initial saturation scale in lead to be $Q_0^2 = N_{\mathrm{part}}^{\mathrm{Pb}} \cdot 0.168\ \mathrm{GeV}^2$, where $N_{\mathrm{part}}^{\mathrm{Pb}}$ denotes the number of nucleon participants on the lead side.

For the analysis of the CMS data, we must be able to make a reasonable estimate of the centrality class based on the total charge particle multiplicity. As this quantity is sensitive to soft particle production we make use of local parton hadron duality:

$$N_{\mathrm{trk}}^{\mathrm{offline}} = \kappa_g \int_{-2.4-y_{\mathrm{shift}}}^{+2.4-y_{\mathrm{shift}}} d\eta \int_{0.4\ \mathrm{GeV}} d^2\mathbf{p}_T \frac{dN}{d\eta d^2\mathbf{p}_T}(\mathbf{p}_T), \quad (7)$$

where κ_g is a gluon liberation factor. The single inclusive gluon distribution in the right-hand side is defined as [4]

$$\frac{\mathrm{d}N_1}{\mathrm{d}y_p \mathrm{d}^2\mathbf{p}_T} = \frac{\alpha_s N_C}{4\pi^6(N_C^2 - 1)} \frac{S_\perp}{\mathbf{p}_T^2} \int_{\mathbf{k}_T} \Phi_{A_1}(y_p, \mathbf{k}_T) \times \Phi_{A_2}(y_p, \mathbf{p}_T - \mathbf{k}_T), \quad (8)$$

where $y_{\mathrm{shift}} = 0.465$ is the shift in rapidity in the center-of-mass frame in asymmetrical p + Pb collisions towards the lead fragmentation region. In Eq. (7), the combination of the transverse overlap area $S_\perp$ times κ_g is fixed (for $Q_0^2 = 0.168\ \mathrm{GeV}^2$ in both protons), from minimum bias proton–proton collisions to give $N_{\mathrm{trk}}^{\mathrm{offline}} = 16$, the value quoted by CMS [1]. This value, $(\kappa_g S_\perp)$, is subsequently held fixed to determine $N_{\mathrm{trk}}^{\mathrm{offline}}$ as Q_0^2 in both the proton and lead nucleus is varied. Admittedly, the constant $S_\perp$ may vary with both beam energy and centrality. This uncertainty would be reflected in a rescaling of the x axis of Fig. 2 and the left plot of Fig. 3. However, we expect these corrections to be small. As shown in Ref. [20] the value of $S_\perp$ varies only logarithmically with beam energy. Furthermore, as discussed later, the interaction cross section is on the order of the size of the proton and not the nucleus.

Part of the analysis of the CMS data requires the calculation of the number of trigger particles, defined here as

$$N_{\rm trig} = \int_{-2.4-y_{\rm shift}}^{+2.4-y_{\rm shift}} d\eta \int_{p_T^{\rm min}}^{p_T^{\rm max}} d^2\mathbf{p}_T \int_0^1 dz \frac{D(z)}{z^2} \frac{dN}{d\eta d^2\mathbf{p}_T}\left(\frac{p_{\rm T}}{z}\right). \tag{9}$$

In Eq. (9), the fragmentation functions are chosen, as in Ref. [9], to be the NLO KPP parametrization [29] for gluon fragmentation to charged hadrons.

The double inclusive multiplicity is computed as

$$\frac{d^2N}{d\Delta\phi} = \int_{-2.4-y_{\rm shift}}^{+2.4-y_{\rm shift}} d\eta_p d\eta_q \mathcal{A}(\eta_p,\eta_q) \times \int_{p_T^{\rm min}}^{p_T^{\rm max}} \frac{dp_T^2}{2} \int_{q_T^{\rm min}}^{q_T^{\rm max}} \frac{dq_T^2}{2} \int d\phi_p \int d\phi_q \delta(\phi_p - \phi_q - \Delta\phi) \times \int_0^1 dz_1 dz_2 \frac{D(z_1)}{z_1^2} \frac{D(z_2)}{z_2^2} \frac{d^2N^{\rm corr}}{d^2\mathbf{p}_T d^2\mathbf{q}_T d\eta_p d\eta_q}\left(\frac{p_{\rm T}}{z_1}, \frac{q_{\rm T}}{z_2}, \Delta\phi\right). \tag{10}$$

Bounds on the range of the trigger and associated hadron momenta are denoted respectively as $p_T^{\min(\max)}$ and $q_T^{\min(\max)}$. Likewise, $\Delta\eta_{\min}(\Delta\eta_{\max}) = 2.0(4.0)$ denote the pseudorapidity gap [30] of hadrons within the experimental acceptance $\mathcal{A}(\eta_p,\eta_q) \equiv \theta(|\eta_p - \eta_q| - \Delta\eta_{\min}) \times \theta(\Delta\eta_{\max} - |\eta_p - \eta_q|)/\mathcal{B}$ where $\mathcal{B} = 2\int_2^4 d\Delta\eta(1 - \Delta\eta/4.8) = 1.5$ takes into account the acceptance of the uncorrelated background.

The associated yield is computed using the zero-yield-at-minimum (ZYAM) procedure,

$$\text{Assoc Yield} = \frac{1}{N_{\rm trig}} \int_0^{\Delta\phi_{\rm min}} d\Delta\phi \left(\frac{d^2N}{d\Delta\phi} - \frac{d^2N}{d\Delta\phi}\bigg|_{\Delta\phi_{\rm min}}\right), \tag{11}$$

where $\Delta\phi_{\rm min}$ is the angle at which the two particle correlation strength is minimal. An important point to note is that the transverse overlap area $S_\perp$ cancels out between the numerator and denominator in the right-hand side eliminating a source of uncertainty in dihadron spectra.

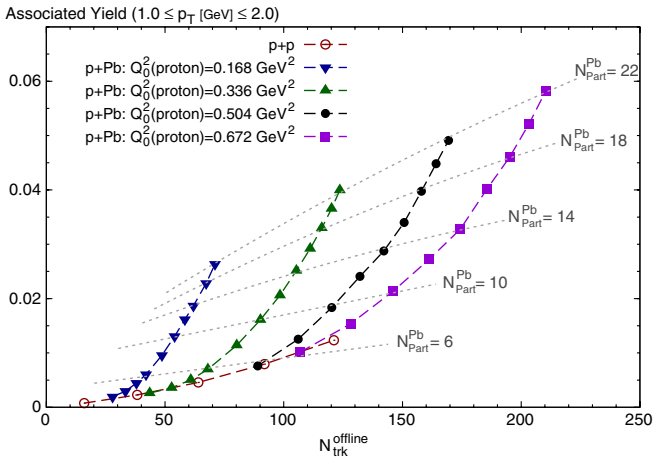

FIG. 2 (color online). The nearside yield per trigger as a function of $N_{\rm trk}^{\rm offline}$ for $1 \le p_T \le 2$, for $p_T = p_T^{\rm trig} = p_T^{\rm asc}$. Each of the p + Pb curves corresponds to a fixed initial saturation scale in the proton. The trajectory of a curve shows how the yield increases with a larger number of participants in the nucleus. The initial saturation scale in the Pb nucleus is related to the number of participants through $Q_0^2(\text{lead}) = N_{\rm part}^{\rm Pb} \cdot 0.168\,\text{GeV}^2$. The values of $Q_0^2(\text{proton}) = 0.168$–$0.672\,\text{GeV}^2$ (the typical saturation scale in the adjoint representation probed in the collisions is on the order $Q_S^2 \approx 0.7$–$2.5\ \text{GeV}^2$) represent estimates of these quantities from median ("minimum bias") impact parameters in the proton to very central impact parameters, respectively.

After these preliminaries, we are now ready to discuss our results. In Fig. 2, we plot the integrated associated nearside yield per trigger [obtained from Eqs. (10) and (11)] versus $N_{\rm trk}^{\rm offline}$ as determined in Eq. (9). The only inputs are $Q_0^2(\text{proton})$ and $Q_0^2(\text{lead}) = N_{\rm part}^{\rm Pb} \cdot 0.168\ \text{GeV}^2$. We first point out that the prediction in our paper [9] for the p + Pb ridge corresponded to $N_{\rm part}^{\rm Pb} = 6$ (which we called "central") for the left most curve [with $Q_0^2(\text{proton}) = 0.168\ \text{GeV}^2$]. Clearly, this signal is close in magnitude to the high multiplicity p + p ridge signal, if one follows the line of sight of the $N_{\rm part}^{\rm Pb} = 6$ grey dashed line. This is similar to the observation in Fig. 3 of Ref. [14], where the signal at $N_{\rm trk}^{\rm offline} = 60$ in p + Pb is comparable to that in p + p at $N_{\rm trk}^{\rm offline} = 100$.

What is particularly striking about Fig. 2 is the large signal one obtains as one cranks up both $Q_0^2(\text{proton})$ and $N_{\rm part}^{\rm Pb}$ in the lead nucleus. As one goes to larger (rarer) values of $N_{\rm trk}^{\rm offline}$, one observes that each of the curves grows rapidly. The number of participants on the lead side is in line with Monte-Carlo Glauber estimates for not especially rare events [31,32]. Interestingly, rarer events are achieved more efficiently by having gluon distributions at more central impact parameters in the proton [larger values of $Q_0^2(\text{proton})$] interact than by adding a larger and larger number of participants on the lead side. As is well known, the multiplicity in p + A collisions grows linearly with increasing the saturation scale in the proton, but only logarithmically with the saturation scale in the nucleus [33], if the latter is the larger of the two [34]. There is also a further effect that when one increases the

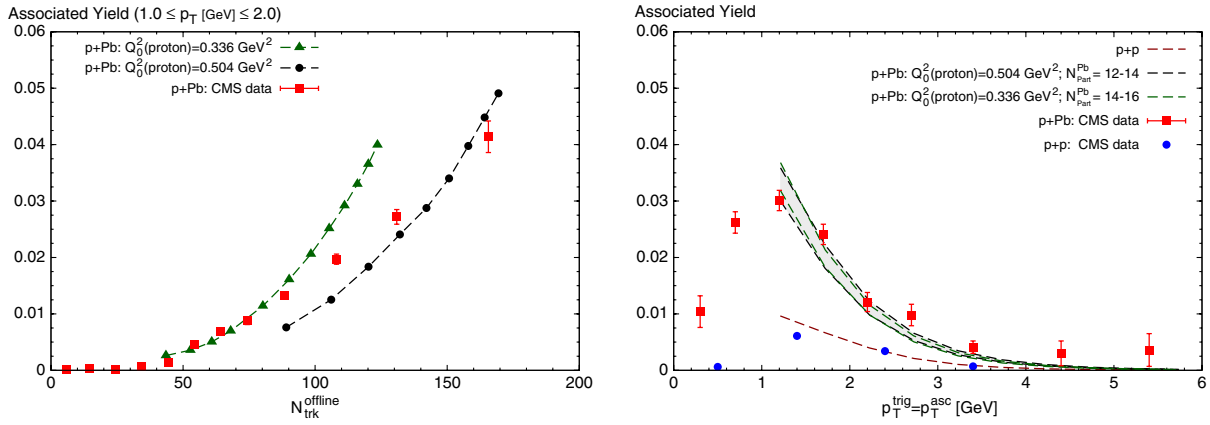

FIG. 3 (color online). Left: The integrated nearside associated yield per trigger as a function of $N_{\rm trk}^{\rm offline}$ for $1 \le p_T \le 2$. The two curves on which data from Ref. [14] are overlaid are the $Q_0^2(\text{proton}) = 0.336$ GeV^2 and $Q_0^2(\text{proton}) = 0.504$ GeV^2 results from Fig. 2. Right: The p_T ($p_T^{\rm trig} = p_T^{\rm asc}$) dependence of the associated yield for the same Q_0^2(proton) values as the previous plot denoted by green (lower) and black (upper) dashed lines, for two different $N_{\rm part}^{\rm Pb}$ ranges. The data here are for $N_{\rm trk}^{\rm offline} \ge 110$ that is approximated (see Fig. 2) by the $N_{\rm part}^{\rm Pb}$ ranges considered.

saturation scale in the nucleus, some of the excess multiplicity is pushed out of the detector acceptance, this acceptance having wider coverage in the lead nucleus fragmentation region. In general, however, one will have a multiplicity distribution with $N_{\rm trk}^{\rm offline}$ generated by a number of different impact parameters in the overlap of proton and lead nuclei, and one needs to average over the signal on the y axis of Fig. 2 with the appropriate weight for a more quantitative analysis. Nevertheless, as seen in the figure, the essential point is that there is no problem obtaining a large associated yield for p + Pb collisions at the LHC for reasonable values of Q_0^2 and $N_{\rm part}^{\rm Pb}$. The reasons for this we will discuss at length in the next section.

In Fig. 3, we show comparisons of computations of the integrated nearside associated yield per trigger with the CMS data from Ref. [14]. In the left plot in this figure, we compare to the data the centrality dependence of the associated yield computed for two different values of Q_0^2(proton) while varying $N_{\rm part}$ on the lead side. These curves are the same as the second and third curves (from left) in Fig. 2, with the same $N_{\rm part}^{\rm Pb}$ values labeling the different points. The p_T distributions (for $p_T^{\rm trig} \simeq p_T^{\rm asc}$) as measured by the CMS collaboration are shown in the right plot of Fig. 3. Also shown is a compilation of four curves from the glasma graph computation obtained by varying the initial saturation scale in the proton from $Q_0^2(\text{proton} = 0.336$ to 0.504 GeV^2 for $N_{\rm part}^{\rm Pb} = 14$ and 16 or $N_{\rm part}^{\rm Pb} = 12$ and 14, respectively. These configurations were chosen to be representative of the $N_{\rm trk}^{\rm offline} \ge 110$ centrality class. Clearly, as noted, a given $N_{\rm trk}^{\rm offline}$ can correspond to different combinations of configurations from the proton and lead side. A more realistic computation would include an average over all multiplicities weighted by the corresponding multiplicity distribution. This caveat aside, we find that the results in Fig. 3 reproduce the $N_{\rm trk}^{\rm offline}$ and p_T dependence of the associated yield rather well.

It is clear at this point that the glasma graphs are able to account for all of the available systematics of the nearside associated yield. We now consider a more differential quantity, the correlated yield as a function of the relative azimuthal angle $\Delta\phi$ between dihadrons having momentum $p_T^{\rm trig}$ and $p_T^{\rm asc}$. In order to fully understand the $\Delta\phi$ dependence, there are three components one must have under control as summarized in Fig. 1: first, the nearside glasma diagrams, which have already been discussed at length. Second, one needs to include the contribution from minijet back-to-back graphs in order to have a quantitative picture of the awayside. As mentioned here, and as shown clearly in our previous work on high multiplicity p + p collisions, dijet production with BFKL evolution between the triggered particles is the right framework for assessing this quantity. Finally, one needs to have control of the underlying event. The underlying event is a true correlation with a distinct $p_T^{\rm trig}$ and $p_T^{\rm asc}$ structure but no angular dependence. However, we know that there are other CGC diagrams [35–38] that may contribute to the underlying event, which do not produce a robust collimation, hence the importance of the ZYAM procedure to remove these contributions. We will briefly discuss some interesting characteristics of the underlying event within our framework.

Figure 4 shows the correlated yield $1/N_{\rm trig} d^2N/d\Delta\phi$ for various ranges of $p_T^{\rm trig}$ and $p_T^{\rm asc}$ and centrality classes after performing the ZYAM procedure in each bin [39]. The shaded band corresponds to one source of uncertainty in our results from the choice of K factors. The curve that appears larger on the awayside corresponds to the K factors obtained from our previous analysis of p + p data

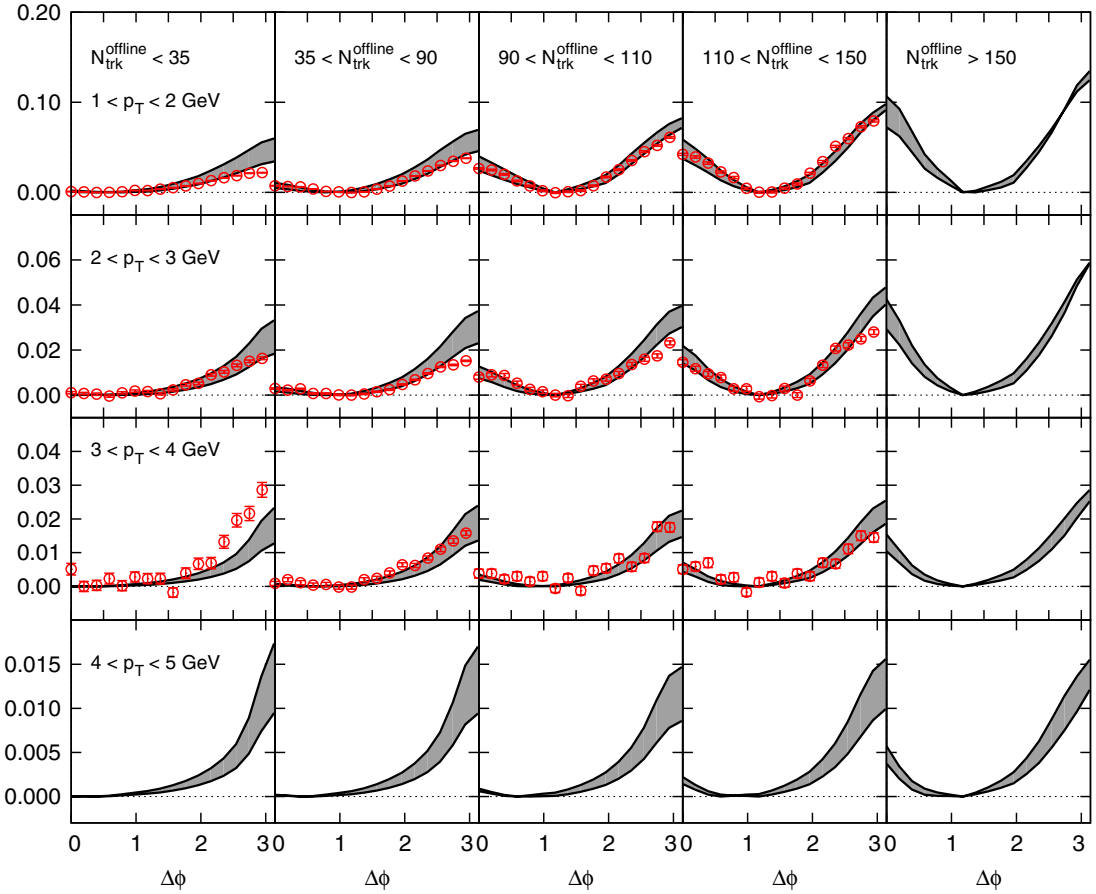

FIG. 4 (color online). Correlated yield $1/N_{\rm trig} d^2N/d\Delta\phi$ after ZYAM as a function of $\Delta\phi$ integrated over $2 \leq |\Delta\eta| \leq 4$ for several multiplicity bins, each for a particular range in $p_T^{\rm trig} = p_T^{\rm asc}$. The data points are from the CMS collaboration [14]. The theoretical curves are the result of adding the glasma and BFKL contributions with the band representing the variation in results when changing the K factors from $K_{\rm glasma} = 1.5$, $K_{\rm bfkl} = 1.65$ to $K_{\rm glasma} = 1.95$, $K_{\rm bfkl} = 0.9$. The results for the different multiplicity windows correspond (from left to right) to $Q_0^2({\rm proton}) = 0.168$ GeV^2, $N_{\rm part}^{\rm Pb} = 3$; $Q_0^2({\rm proton}) = 0.336$ GeV^2, $N_{\rm part}^{\rm Pb} = 6$; $Q_0^2({\rm proton}) = 0.336$ GeV^2, $N_{\rm part}^{\rm Pb} = 12$; $Q_0^2({\rm proton}) = 0.504$ GeV^2, $N_{\rm part}^{\rm Pb} = 14$; $Q_0^2({\rm proton}) = 0.504$ GeV^2, $N_{\rm part}^{\rm Pb} = 22$. Predictions are shown for very large multiplicity windows and higher values of $p_T^{\rm trig} = p_T^{\rm asc}$.

($K_{\rm glasma} = 1.5$ and $K_{\rm bfkl} = 1.65$) with the other curve corresponding to a new choice (fit by eye) of $K_{\rm glasma} = 1.95$ and $K_{\rm bfkl} = 0.9$. The centrality dependence of the result is controlled by our selection of representative values of both $Q_0^2({\rm proton})$ and $N_{\rm part}^{\rm Pb}$ that approximately reproduce the mean multiplicity in each centrality class.

In Fig. 5, we show results for the highest multiplicity events. CMS p + Pb data is only available at present for three of these windows diagonal in $p_T^{\rm trig} \sim p_T^{\rm asc}$, shown as the red data points. The curves are the sum of the glasma contribution and the BFKL contribution. The solid black curve is the result for $Q_0^2({\rm proton}) = 0.504$ GeV^2 on $N_{\rm part}^{\rm Pb} = 14$ and the dashed green is for $Q_0^2({\rm proton}) = 0.336$ GeV^2 on $N_{\rm part}^{\rm Pb} = 16$. As before, we have chosen these values to be representative of the $N_{\rm trk}^{\rm offline} \geq 110$ centrality class. A more quantitative result could in principle be obtained by the appropriate averaging over various events as discussed earlier. The K factors were chosen to coincide with those extracted from our previous analysis of p + p collisions ($K_{\rm glasma} = 1.5$ and $K_{\rm bfkl} = 1.65$). There is no reason why these should not be adjusted to p + Pb collisions [40].

The differential associated yields show that the combination of glasma and BFKL dynamics provides quite a good description of the data without too much fine tuning. The K factors for glasma and BFKL graphs used previously for the high multiplicity p + p results do a good job in many windows of the matrix in Fig. 4 but tend to overpredict the BFKL contribution in some of the windows. Reasonable changes in K values, as shown by the band, are likely to give a finer tuned description of these ~200 data points along with the additional several hundred data points of p + p data all with K values of order unity.

As shown in Fig. 5, the systematics of the awayside signal becoming dominated by the "dipole"-like glasma graphs in high multiplicity events is reproduced. It is very

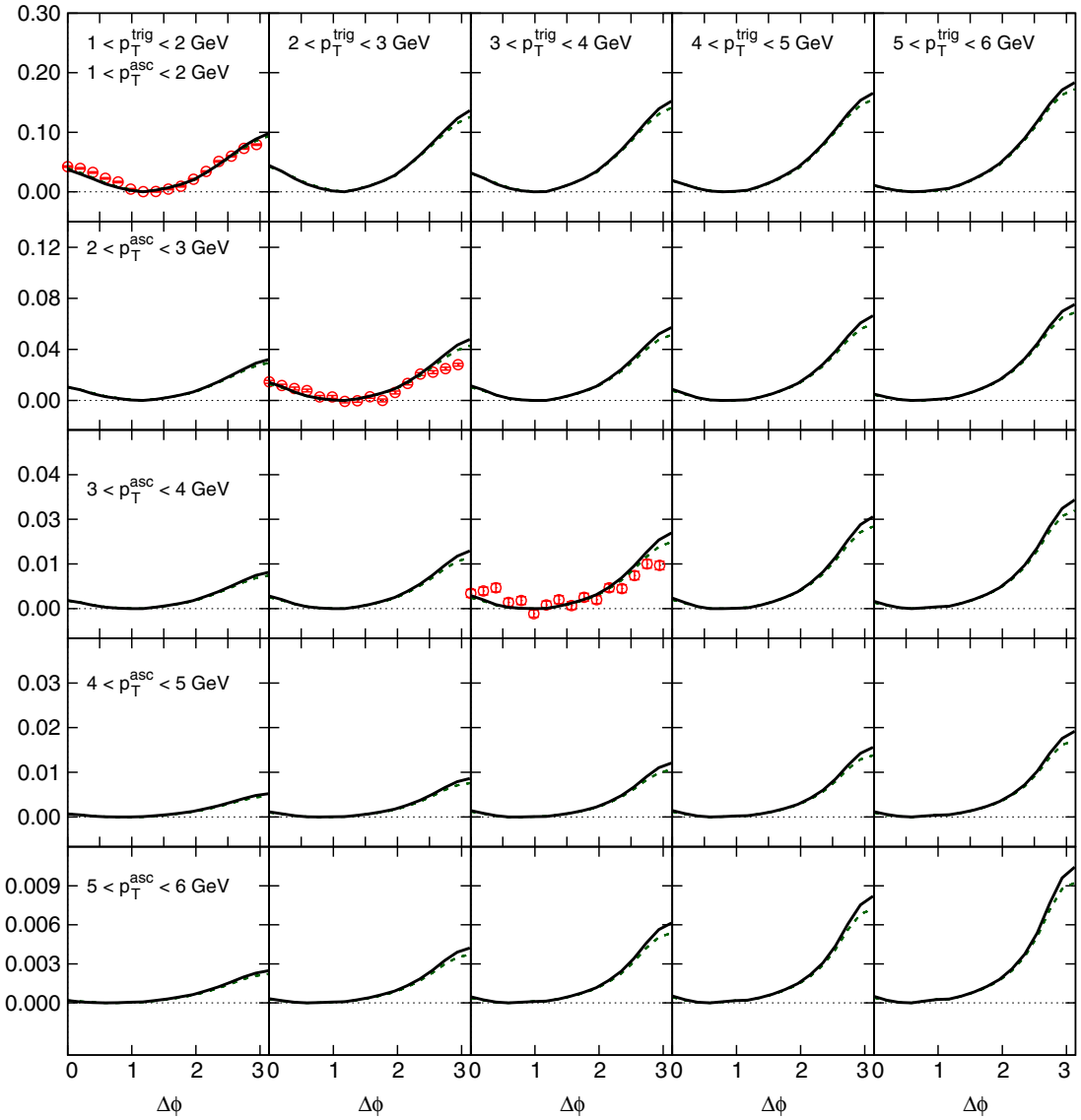

FIG. 5 (color online). Correlated yield $1/N_{\rm trig} d^2N/d\Delta\phi$ after ZYAM as a function of $\Delta\phi$ integrated over $2 \leq |\Delta\eta| \leq 4$ for the most central multiplicity bin $N_{\rm trk}^{\rm offline} \geq 110$. The data points are from the CMS collaboration [14] and have currently only been provided for the diagonal components $p_T^{\rm trig} \sim p_T^{\rm asc}$ of the correlation matrix. The curves are obtained by adding the glasma contributions ($K = 1.5$) and the BFKL contribution ($K = 1.65$). The solid black curve is the result for $Q_0^2({\rm proton}) = 0.504$ GeV^2 on $N_{\rm part}^{\rm Pb} = 14$ and the dashed green is for $Q_0^2({\rm proton}) = 0.336$ GeV^2 on $N_{\rm part}^{\rm Pb} = 16$.

nontrivial that the BFKL awayside dynamics is suppressed in awayside events such that the combination of Glasma + BKFL on the awayside does not overestimate the awayside signal. This happens because the BFKL dijet yield per trigger is very weakly dependent on $N_{\rm part}$ since the UGDs in the numerator of Eq. (5) are the same as in the expression for $N_{\rm trk}^{\rm offline}$ in Eq. (9).

Finally, it is interesting to examine the $N_{\rm trk}^{\rm offline}$ dependence of the correlated $\Delta\phi$-independent yield. Figure 6 (left) demonstrates that the yield depends on $N_{\rm trk}^{\rm offline}$ alone for differering values of $Q_0^2({\rm proton})$ and $N_{\rm part}$, while the collimated signal shown in Fig. 2 clearly has a more complex structure. In particular, unlike the case of the collimated yield, the p + p and p + Pb underlying event contributions lie on the same curve. Also shown in Fig. 6) are the data points for $C_{\rm ZYAM}$ from Ref. [14] divided by a factor of 5. It is very interesting that the data follow the same $N_{\rm trk}^{\rm offline}$ scaling as the glasma graphs. The BFKL contribution to the associated yield is shown in Fig. 6 (right). It clearly does not have the same $N_{\rm trk}^{\rm offline}$ scaling, and is approximately of the same magnitude as the glasma underlying event at $N_{\rm trk}^{\rm offline} \sim 100$. However, as we noted previously [9], recent computations [27,41] show that the ϕ-independent NLLx contributions are a factor of 2–3 *below* the LLx contribution [42]. Hence, there is ample room for other contributions in the CGC that only produce

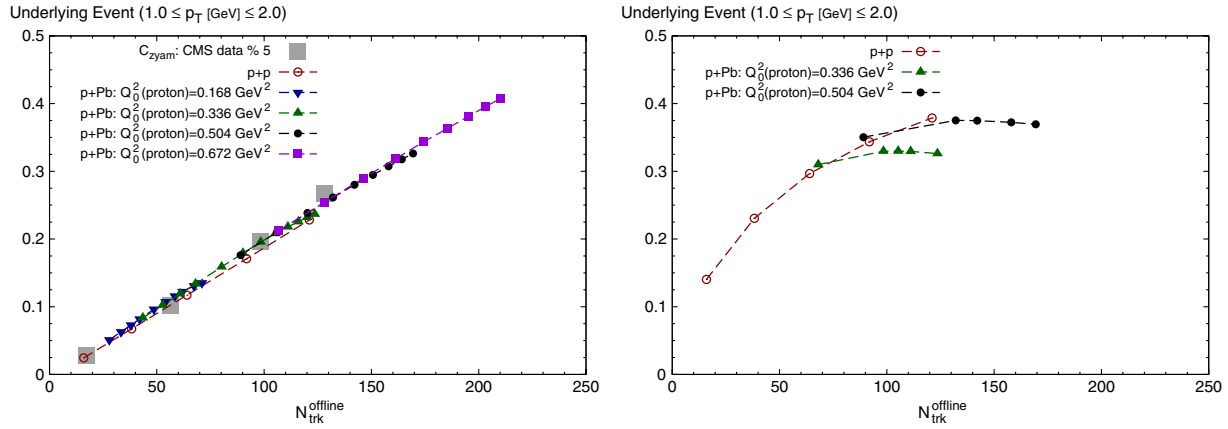

FIG. 6 (color online). Left: The underlying glasma event per trigger (equivalent to $C_{\rm zyam}$ in Ref. [14]) as a function of $N_{\rm trk}^{\rm offline}$ for $1 \le p_T^{\rm trig}, p_T^{\rm asc} \le 2$. The large grey squares are the experimental values of $C_{\rm ZYAM}$ divided by a factor 5. All other symbols denote theory computations with a fixed initial scale Q_0 in the proton and varying values of $N_{\rm part}^{\rm pPb}$. Right: The underlying BFKL event per trigger for $Q_0^2 = 0.336$ GeV^2 and $Q_0^2 = 0.504$ GeV^2 and varying values of $N_{\rm part}$. See text for discussion.

a $\Delta\phi$-independent contribution [35–38] as long as they give the same scaling as the glasma graphs.

IV. DISCUSSION AND OUTLOOK

We showed in the previous section that the CGC EFT gives a good description of the novel systematics of proton-lead dihadron correlations that are long range in rapidity and collimated in the azimuthal angle. This is important because an identical analysis previously gave very good agreement with the CMS data for dihadron correlations in high multiplicity p + p events. We conclude that the origins of the proton-lead effect are the same as the one in proton-proton collisions and unlike nucleus-nucleus collisions, where the systematics of the associated yield is dominated by flow [4]. A simple but apt analogy that exemplifies our conclusion is that a bullet shot through a plane of glass has an interaction cross section closer to the size of the bullet and not that of the glass.

But what is the deeper origin of the effect? The systematic features of the comparison to data are consistent with the following picture of the proton-lead interaction. As shown previously [20,43] on the basis of HERA electron-proton diffractive data, the saturation scale in the proton has a strong impact parameter dependence which we have modeled here with different values of Q_0^2(proton). In proton-proton collisions, Q_0^2(proton) = 0.168 GeV^2, the value at the median impact parameter is more likely; rare events that correspond to the higher Q_0^2 which produces the high multiplicity collisions (and the ridge) are very unlikely. In contrast, in a proton-lead collision, any given $N_{\rm trk}^{\rm offline}$ has a higher probability to be generated by a larger Q_0^2(proton) than the median value. This is because the likelihood that gluons at small impact parameters in the proton interact is much larger when the proton is scattering off many nucleons along its path, as in a lead nucleus. Such events are more likely to dominate the probability P_N for a given $N_{\rm trk}^{\rm offline}$. That would explain why the values of the associated yield seen in Fig. 3 are more compatible with the larger Q_0^2(proton) values.

The prior discussion addresses why larger Q_0^2(proton) are more relevant for a given $N_{\rm trk}^{\rm offline}$. But it does not explain why the associated yield is so large in p + Pb for any Q_0^2(proton) as one varies Q_0^2(lead) as shown in Fig. 2. The underlying reason is a subtle form of quantum entanglement. To simplify the discussion, we will consider only

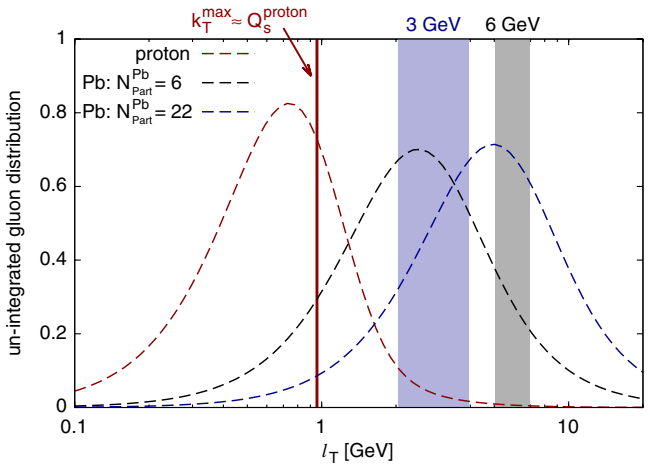

FIG. 7 (color online). The UGD of a min. bias proton [Q_0^2(proton) = 0.168 GeV^2] and for lead nuclei for two different values of $N_{\rm part}$. The former is evolved to rapidity $Y = 1$ and the latter are evolved to $Y = 4$. The red vertical line $k_T \sim Q_s$ (proton) denotes the peak of the integrand in Eq. (12). The remaining angular integral in Eq. (12) is constrained by kinematics to lie within the blue (gray) shaded region for $|\mathbf{p}_T| =$ 3(6) GeV. The collimated signal is determined by the curvature in the shaded regions—flat UGDs are uncollimated.

one of the glasma diagrams responsible for the nearside collimation evaluated [44] at $y_p = y_q = 0$. In this case, the two particle correlation is proportional to

$$d^2N \propto S_\perp \int d^2k_\perp \Phi_A^2(\mathbf{k}_T)\Phi_B(|\mathbf{p}_T - \mathbf{k}_T|)\Phi_B(|\mathbf{q}_T - \mathbf{k}_T|). \tag{12}$$

To ascertain why the above expression yields a signal that is collimated, namely, a larger signal for $\mathbf{p}_T = \mathbf{q}_T$ as opposed to the signal when $\mathbf{p}_T \neq \mathbf{q}_T$, let us consider for simplicity $|\mathbf{p}_T| = |\mathbf{q}_T|$. This condition, and application of the Cauchy-Schwarz inequality [45] leads to the condition

$$\int d^2k_\perp \Phi_A^2(\mathbf{k}_T)\Phi_B(|\mathbf{p}_T - \mathbf{k}_T|)\Phi_B(|\mathbf{q}_T - \mathbf{k}_T|) \leq \int d^2k_\perp \Phi_A^2(\mathbf{k}_T)\Phi_B^2(|\mathbf{p}_T - \mathbf{k}_T|). \tag{13}$$

When the equality holds, there is clearly no collimation because the rhs does not depend on $\Delta\phi_{pq}$. However, the equality holds if and only if $\Phi(|\mathbf{p}_T + \mathbf{k}_T|) \propto \Phi(|\mathbf{q}_T + \mathbf{k}_T|)$, which is only satisfied if the un-integrated gluon distribution is flat within the available phase space. Figure 7 clearly shows that the unintegrated gluon distributions are not flat. Therefore, on very general grounds, we expect a collimation from the structure of the two particle correlation in Eq. (12).

Now that we have argued on very general grounds that there must be a collimation, we would like to understand the scaling of the yield with $N_{\rm trk}^{\rm offline}$ and $N_{\rm part}$ as seen in Fig. 2. As seen in Fig. 6, the underlying event (which characterizes the overall normalization of the signal) scales linearly with $N_{\rm trk}^{\rm offline}$. Any $N_{\rm trk}^{\rm offline}$ dependence in Fig. 2 is therefore a consequence of the $N_{\rm trk}^{\rm offline}$ scaling of the normalization. In addition to this $N_{\rm trk}^{\rm offline}$ scaling, there is a ridge collimation that grows rapidly with $N_{\rm part}$. We will now discuss in turn both aspects of the systematics of the observed signal.

From the previous discussion, the underlying event has the form

$$\mathrm{UE} \propto \frac{\int d^2k_\perp \Phi_A^2(\mathbf{k}_T)\Phi_B^2(|\mathbf{p}_T - \mathbf{k}_T|)}{\int d^2k_\perp \Phi_A(\mathbf{k}_T)\Phi_B(|\mathbf{p}_T - \mathbf{k}_T|)}, \tag{14}$$

where the term in the denominator is itself proportional to $N_{\rm trk}^{\rm offline}$. Because the Φ's, as shown in Fig. 7, are bell shaped curves peaked about the saturation scales, one can deduce by inspection [46] that the numerator scales as $(N_{\rm trk}^{\rm offline})^2$, and hence the UE $\propto N_{\rm trk}^{\rm offline}$.

We now address the additional $N_{\rm part}$ scaling that is observed only in the collimated associated yield (CY). This can be characterized by looking at that ratio of the signal from Eq. (12) evaluated in Ref. [47] $\Delta\phi_{pq} = 0$ to that at $\Delta\phi_{pq} = \pi$ for $|\mathbf{p}_T| = |\mathbf{q}_T|$,

$$\mathrm{CY} \propto \frac{\int d^2k_\perp \Phi_A^2(\mathbf{k}_T)\Phi_B^2(|\mathbf{p}_T - \mathbf{k}_T|)}{\int d^2k_\perp \Phi_A^2(\mathbf{k}_T)\Phi_B(|\mathbf{p}_T - \mathbf{k}_T|)\Phi_B(|\mathbf{p}_T + \mathbf{k}_T|)}. \tag{15}$$

The $N_{\rm trk}^{\rm offline}$ scaling cancels in this ratio. To see simply how the additional collimation arises, consider the extreme scenario where the Φs are peaked strongly enough to be considered Dirac delta distributions. Working within this approximation we can easily perform the integral over $d^2k_\perp$, whereby $\Phi_A^2(\mathbf{k}_T)$ fixes $|\mathbf{k}_T| = Q_A$ and the angular integral over $\Phi_B(|\mathbf{p}_T - \mathbf{k}_T|)$ fixes

$$\phi = \arccos\left(\frac{Q_B^2 - Q_A^2 - p_T^2}{2p_T Q_A}\right). \tag{16}$$

After making these substitutions [48], we are left with

$$\mathrm{CY} \propto \frac{\Phi_B(Q_B)}{\Phi_B(\sqrt{2p_T^2 + 2Q_A^2 - Q_B^2})}. \tag{17}$$

The collimated signal is always larger than unity [49] since the maximum of Φ_B is at Q_B. As Q_B is increased (while keeping p_T and Q_A fixed) the wave function in the denominator is probed further away from its maximum leading to a larger collimation. If we make a Gaussian approximation for the remaining wave functions in Eq. (17), we find a rapid growth in the collimated signal with $N_{\rm part}$. For the region where $Q_B \gtrsim Q_A$, we find

$$\mathrm{CY} \propto 1 + \frac{1}{Q_A^2}(Q_B - Q_A)^2, \tag{18}$$

which grows as $\sim N_{\rm part}$.

To summarize the discussion, the behavior of the associated yield is a consequence of the quantum entanglement of the wave functions of correlated gluons in both the projectile and the target. Since two gluons from both projectile and target participate, one obtains the overlap of four wave functions. Besides energy-momentum constraints on the wave functions, the signal is sensitive to the detailed structure of these wave functions. This includes both the density of gluons with varying impact parameter, as well as the p_T dependence of the gluon distributions for a fixed impact parameter. With the stated simple yet fairly general assumptions, the scaling of the collimated yield and the underlying event as a function of $N_{\rm trk}^{\rm offline}$ and $N_{\rm part}$ is reproduced. The physics of saturation is absolutely crucial: first, on a "global" level because the glasma graphs are tremendously enhanced due to the large phase space occupancy of gluons, but equally so because the observed signal is sensitive to detailed features of the CGC EFT.

The theoretical framework employed here can be further improved. An important step is to self-consistently include multiple scattering effects alongside the rapidity evolution of two gluon production. The framework to do this has been developed but not implemented numerically yet [23]. Another improvement is to quantify the

NLLx contributions to the collimated yield and the underlying event for the kinematics of interest [27,41]. Not least, the contributions of leading N_c multigluon correlators and possible pomeron loop effects need to be quantified [3].

Finally, while this work was in preparation, a preprint appeared which interprets the effect as due to hydrodynamic flow [50]. As noted previously, we believe the ridge in p + Pb collisions to be more analogous to high multiplicity p + p collisions than Pb + Pb collisions: the systematics of the study here lends weight to this conclusion. For the p + p case, we showed that inclusion of flow [4] changes the structure of the associated yield from that observed in the data even for modest flow velocities. While some multiple scattering cannot be categorically ruled out, a consistent hydrodynamic description is challenging for systems with transverse sizes the order of the proton size because of poor convergence of the gradient expansion and the short lifetime of the system. It will be interesting to see whether the hydrodynamic description of Bozek and Broniowski [50] holds for a wider p_T and centrality range than shown. In this regard, it is important that one include the nonflow jet-like BFKL contribution that provides a significant contribution to the awayside yield.

ACKNOWLEDGMENTS

K. D. and R. V. are supported by the U.S. Department of Energy under DOE Contracts No. DE-FG02-03ER41260 and No. DE-AC02-98CH10886, respectively. This research used resources of the National Energy Research Scientific Computing Center, which is supported by the Office of Science of the U.S. Department of Energy under Contract No. DE-AC02-05CH11231. We would like to acknowledge useful conversations with Adam Bzdak, Adrian Dumitru, Alex Kovner, Wei Li, and Larry McLerran.

[1] V. Khachatryan *et al.* (CMS Collaboration), J. High Energy Phys. 9 (2010) 091.
[2] W. Li, Mod. Phys. Lett. A **27**, 1230018 (2012).
[3] A. Kovner and M. Lublinsky, arXiv:1211.1928 [Int. J. Mod. Phys. (to be published)].
[4] K. Dusling and R. Venugopalan, Phys. Rev. Lett. **108**, 262001 (2012).
[5] A. Dumitru, F. Gelis, L. McLerran, and R. Venugopalan, Nucl. Phys. **A810**, 91 (2008).
[6] K. Dusling, F. Gelis, T. Lappi, and R. Venugopalan, Nucl. Phys. **A836**, 159 (2010).
[7] A. Dumitru, K. Dusling, F. Gelis, J. Jalilian-Marian, T. Lappi, and R. Venugopalan, Phys. Lett. B **697**, 21 (2011).
[8] F. Gelis, E. Iancu, J. Jalilian-Marian, and R. Venugopalan, Annu. Rev. Nucl. Part. Sci. **60**, 463 (2010).
[9] K. Dusling and R. Venugopalan, arXiv:1210.3890 [Phys. Rev. D (to be published)].
[10] L. Gribov, E. Levin, and M. Ryskin, Phys. Rep. **100**, 1 (1983).
[11] A. H. Mueller and J.-w. Qiu, Nucl. Phys. **B268**, 427 (1986).
[12] I. Balitsky and L. Lipatov, Sov. J. Nucl. Phys. **28**, 822 (1978).
[13] E. Kuraev, L. Lipatov, and V. S. Fadin, Sov. Phys. JETP **45**, 199 (1977).
[14] S. Chatrchyan *et al.* (CMS Collaboration), Phys. Lett. B **718**, 795 (2013).
[15] Here onwards we will use the CMS notation $N_{\mathrm{trk}}^{\mathrm{offline}}$ to discuss the number of charged hadron tracks. Our results will be normalized to the same by equating our multiplicities to their values for the same in minimum bias proton-proton collisions. This point is discussed further on in the text.
[16] As previously in Ref. [9], the delta distribution is smeared as $\delta(\phi_{pq}) \to \frac{1}{\sqrt{2\pi}\sigma} e^{-\phi_{pq}^2/2\sigma^2}$, where $\Delta\phi_{p,q} = \phi_p - \phi_q$ and $\sigma = 3$ GeV/$\mathbf{p}_T$ is a $\mathbf{p}_T$ dependent width on the order of the saturation scale. The associated yield—the integral over the nearside signal—is insensitive to details of this smearing.
[17] I. Balitsky, Nucl. Phys. **B463**, 99 (1996).
[18] Y. V. Kovchegov, Phys. Rev. D **60**, 034008 (1999).
[19] J. L. Albacete, N. Armesto, J. G. Milhano, P. Quiroga-Arias, and C. A. Salgado, Eur. Phys. J. C **71**, 1705 (2011).
[20] P. Tribedy and R. Venugopalan, Nucl. Phys. **A850**, 136 (2011).
[21] P. Tribedy and R. Venugopalan, Phys. Lett. B **710**, 125 (2012); **718**, 1154(E) (2013).
[22] B. Schenke, P. Tribedy, and R. Venugopalan, Phys. Rev. C **86**, 034908 (2012).
[23] F. Gelis, T. Lappi, and R. Venugopalan, Phys. Rev. D **79**, 094017 (2009).
[24] A. Dumitru, J. Jalilian-Marian, T. Lappi, B. Schenke, and R. Venugopalan, Phys. Lett. B **706**, 219 (2011).
[25] I. Balitsky, Phys. Rev. D **75**, 014001 (2007).
[26] T. Lappi, S. Srednyak, and R. Venugopalan, J. High Energy Phys. 1 (2010) 066.
[27] D. Colferai, F. Schwennsen, L. Szymanowski, and S. Wallon, J. High Energy Phys. 12 (2010) 026.
[28] V. S. Fadin, M. Kotsky, and L. Lipatov, arXiv:hep-ph/9704267.
[29] B. A. Kniehl, G. Kramer, and B. Potter, Nucl. Phys. **B582**, 514 (2000).
[30] Replacing the rapidity y with the pseudorapidity η is a good approximation for the p_T, q_T of interest.
[31] P. Bozek, Phys. Rev. C **85**, 014911 (2012).
[32] J. L. Albacete, A. Dumitru, H. Fujii, and Y. Nara, Nucl. Phys. **A897**, 1 (2013).
[33] A. Dumitru and L. D. McLerran, Nucl. Phys. **A700**, 492 (2002).

[34] We have checked that this scaling is approximately satisfied by our computed single inclusive multiplicity.
[35] A. Dumitru and J. Jalilian-Marian, Phys. Rev. D **81**, 094015 (2010).
[36] A. Dumitru, J. Jalilian-Marian, and E. Petreska, Phys. Rev. D **84**, 014018 (2011).
[37] A. Kovner and M. Lublinsky, Phys. Rev. D **83**, 034017 (2011).
[38] A. Kovner and M. Lublinsky, Phys. Rev. D **84**, 094011 (2011).
[39] Data is also available for $p_T < 1$ GeV; we have not compared the theory predictions to data in this window because the theory systematic errors are large.
[40] There is a genuine subtlety in comparison of the glasma graph K factors in p + p and p + Pb. In Fig. 2 of Ref. [9], the BFKL contribution on the *nearside* is ZYAM'ed out and the glasma contribution alone with $K = 1.5$ gives a good fit to data. In Fig. 4, for the matrix, as discussed in the text of Ref. [9], the BFKL contribution gives a tiny (relative to awayside) nearside "anticollimation" which is compensated by cranking up the glasma K factor to 3.45. However, the BFKL calculation is not reliable on the nearside and further, it contaminates the tiny but unmistakable glasma signal. If we make it flat from 0 to $\Delta\phi \sim \pi/2$, all the systematics of p + p (as in Fig. 2 of Ref. [9]) would be reproduced with a glasma K factor of 1.5. In the p + Pb case, because the glasma signal is so large for high multiplicity windows, the uncertainties in BFKL on the nearside are of not much import and glasma $K = 1.5$ works quite well.
[41] F. Caporale, D. Y. Ivanov, B. Murdaca, and A. Papa, in The International Workshop "Diffraction 2012," Puerto del Carmen, Spain, 2012 (unpublished).
[42] This may be contrasted to the collimated NLLx contributions that are 10%–30% corrections to LLx, and will be significantly accounted for already by the running coupling effects we have included.
[43] H. Kowalski, L. Motyka, and G. Watt, Phys. Rev. D **74**, 074016 (2006).
[44] For the qualitative arguments in this section, this assumption is sufficient because the glasma signal, to first approximation, is boost invariant.
[45] Define $f(\mathbf{k}_T) = \Phi_A(\mathbf{k}_T)\Phi_B(|\mathbf{p}_T + \mathbf{k}_T|)$ and $g(\mathbf{k}_T) = \Phi_A(\mathbf{k}_T)\Phi_B(|\mathbf{q}_T + \mathbf{k}_T|)$. The two-dimensional form of the Cauchy-Schwarz inequality is

$$\int d^2k_\perp f(\mathbf{k}_T)g(\mathbf{k}_T) \le \sqrt{\int d^2\mathbf{k}_T |f(\mathbf{k}_T)|^2}\sqrt{\int d^2\mathbf{k}_T |g(\mathbf{k}_T)|^2}$$

with the equality holding iff $f(\mathbf{k}_T) \propto g(\mathbf{k}_T)$.
[46] This is confirmed by a simple analysis treating the Φ's as Gaussian wave functions.
[47] In addition to Eq. (12), there is a contribution that has a maximum at π and a minimum at 0. Its the sum of the two contributions that gives the "dipole"-like signal with a minimum at $\pi/2$.
[48] Jacobian factors cancel between numerator and denominator.
[49] The square root in the denominator implies finite support for Q_B in the narrow range $1 \le Q_B/\sqrt{2p_T^2 + 2Q_A^2} \le \sqrt{2}$, which is an artifact of taking Delta function approximation for the wave functions.
[50] P. Bozek and W. Broniowski, Phys. Lett. B **718**, 1557 (2013).